



Full Length Article

Short-range order effects on the thermodynamic behavior of $\text{Al}_x\text{CoCrFeNi}$ high-entropy alloysMd Abdullah Al Hasan^a, Seungha Shin^{a,*}, Peter K. Liaw^b^a Department of Mechanical, Aerospace and Biomedical Engineering, The University of Tennessee, Knoxville, TN, USA^b Department of Materials Science and Engineering, The University of Tennessee, Knoxville, TN, USA

ARTICLE INFO

Keywords:

High-entropy alloys
Short-range order
Thermodynamic property
Molecular dynamics
Monte-Carlo
First-principles calculations

ABSTRACT

Short-range order (SRO) in high-entropy alloys (HEAs) has been observed both computationally and experimentally in recent studies. Despite their recognized influence on the physical properties of the HEAs reported, a comprehensive work on the relationship between SRO and the tuning of the thermodynamic properties of HEAs has been lacking. In this research, to identify the SRO-property relationship, the Warren-Cowley (WC) parameters, which quantify the degree of SRO, and thermodynamic properties in $\text{Al}_x\text{CoCrFeNi}$ HEAs were investigated, utilizing the molecular dynamics (MD) simulations, hybrid molecular dynamics/Monte Carlo (MD/MC) simulations, and density functional theory (DFT) calculations. We examined SROs in different phases of $\text{Al}_x\text{CoCrFeNi}$ HEAs by varying aluminum (Al) contents (x_{Al}) ranging from 0 to 2.0. Results reveal a prevalent negative SRO of Al-Fe and positive SRO of Al-Al pairs across all HEA cases. Under the influence of SRO parameters, lattice thermal conductivity and bulk modulus exhibit higher values, whereas coefficient of thermal expansion exhibits lower values. This research advances our understanding of the SRO-properties relationship in HEAs, contributing to the design of HEAs with tailored properties through structural tuning.

1. Introduction

High-entropy alloys (HEAs), which are a novel class of materials containing at least five principal elements [1–3], have attracted enormous research attention because of their unparalleled compositional varieties and exceptional physical, mechanical, chemical, and magnetic properties, compared to traditional alloys [2–6]. These unique properties of HEAs are attributed to their high mixing entropy that stabilizes the random solid solutions [5–9]. Recent studies reported that not only high configurational entropy but high atomic-level stresses originating from mixing various sizes of elements are also of equal importance [5,9–12]. The chemical interaction and atomic-size mismatch often trigger short-range order (SRO) of atomic elements in HEAs, i.e., the preference for certain types of atomic pairing over the first few neighboring shells [11–15].

Short-range ordering in an alloy can affect the system energetics, changing the configurational entropy, free energy, phase diagram, and enthalpy [14,16]. The SRO was also claimed to be one of the key components influencing various structural and mechanical properties of the HEAs. For example, higher tensile strength in CoCrFeNiPd HEAs [17]

and higher mechanical yield strength in CrCoNi alloys have been observed along with the presence of SROs [16,18]. Therefore, the formation of SROs and their effects on the properties need to be studied and identified for the enhanced understanding and design of HEAs. However, the studies on the SRO in HEAs are very limited in number due to challenges in dealing with the experimental complexities and in interpreting the pair correlations [17,19]. Despite the challenges in experimentally probing SROs, recent measurements using aberration-corrected transmission electron microscopy (TEM) provided direct evidence that various degrees of SROs exist in $(\text{HfNbTiZr})_{98}\text{O}_2$, CoCrFeNiMn , and CoCrFeNiPd [17,20].

In the quest for understanding SROs, several computational techniques have been employed, including the hybrid density functional theory/Monte Carlo (DFT/MC) [13,15,16]. SROs between Ni-Cr, Cr-Co, and Ni-Fe pairs in NiCrCo and NiCrCoFe alloys [16], and Ta-Mo and Nb-Mo pairs in refractory Mo-Nb-Ta-W HEAs [13,15] have been reported from computational research using DFT/MC. Despite recent progress, studies using DFT/MC suffer from expensive computational cost, especially with large atomic structures. Classical molecular dynamics (MD) allows for simulations with a much larger number of atoms while

* Corresponding author.

E-mail address: sshin@utk.edu (S. Shin).<https://doi.org/10.1016/j.commatsci.2024.112980>

Received 4 February 2024; Received in revised form 21 March 2024; Accepted 24 March 2024

Available online 30 March 2024

0927-0256/© 2024 Elsevier B.V. All rights reserved.

addressing atomic structures and dynamic behaviors [21–23]. Through hybrid MD/MC simulations, strong chemical ordering between Fe and Ti was observed in $\text{Co}_{30}\text{Fe}_{16.67}\text{Ni}_{36.67}\text{Ti}_{16.67}$, and their effect on dislocation mobility was analyzed [22]. Without first-principles calculations, a force field or interatomic potential needs to be computed by a mathematical model. However, reliable interatomic potential models for multi-element materials are limited, and the development and validation of such potential models require significant effort.

$\text{Al}_x\text{CoCrFeNi}$ is one of the most studied HEAs since it possesses a wide variety of microstructures depending on Al concentration, which can induce desired mechanical, thermal, and thermodynamic properties [24–26]. $\text{Al}_x\text{CoCrFeNi}$ HEA showcases exceptional overall performance and structural applicability when compared to HEA families, i.e., refractory HEAs and CoCrFeNi-based HEAs due to phase changing capability with the addition of Al content [25]. The impact of SRO on the mechanical and thermodynamic properties is crucial to design further improved $\text{Al}_x\text{CoCrFeNi}$ HEAs to function as a combination of efficient structural materials and functional materials, especially for marine applications, biomedical applications, aerospace applications, and so on [27–29]. A good combination of mechanical and tribological properties in $(\text{NiAl})_x(\text{FeCr})_y\text{Co}_{(x+y)/2}$ HEAs has been achieved via adjusting A2/B2 nano-coupled heterostructures [30], where SROs of Fe-Co, Ni-Al, and Fe-Cr are enriched. Moreover, significant short-range orders around Al atoms were observed even at high temperatures ($\sim 1200^\circ\text{C}$) in the disordered body-centered cubic (BCC) phase of $\text{Al}_x\text{CoCrFeNi}$ HEA ($0.875 < x_{\text{Al}} \leq 2$) [31]. Although the SRO relationship with the mechanical properties of $\text{Al}_x\text{CoCrFeNi}$ HEAs have been reported [30,32], SRO effect on their thermodynamic properties, specifically thermal conductivity, thermal expansion coefficient, and bulk modulus have not been studied to our best knowledge. Additionally, the thermal transport and thermoelectric properties of $\text{Al}_x\text{CoCrFeNi}$ HEAs ($0 \leq x_{\text{Al}} \leq 2.0$) have been examined in several studies [33,34]; however, they only addressed the effects of Al content without considering SROs.

In this research, we employed a combination of atomistic modeling techniques, such as molecular dynamics (MD), Monte Carlo (MC), and density functional theory (DFT), to investigate the effect of local atomic order or short-range order (SRO) on different types of thermodynamic properties, including lattice thermal conductivity, thermal expansion coefficient, and bulk modulus of $\text{Al}_x\text{CoCrFeNi}$ HEAs. The degree of SRO for various atomic pairs was quantified, and the frequencies of atomic orders and their relationship with the examined thermodynamic properties were analyzed. For more robust analysis, several Al contents in $\text{Al}_x\text{CoCrFeNi}$ HEAs ($0 \leq x_{\text{Al}} \leq 2$) were employed, addressing the SRO-property correlations in different compositions. This paper first introduces atomic configurations of the examined face-centered cubic (FCC) and body-centered cubic (BCC) HEAs and provides the atomistic simulation details, characterization methods for SRO and then calculation of thermodynamic properties. Then, the characteristics of the SRO parameters and their correlations to the thermodynamic properties are determined, and effective design of HEAs using the SRO parameters is

discussed.

2. Methodology

2.1. Atomic configurations of $\text{Al}_x\text{CoCrFeNi}$ HEAs

Several Al contents ($x_{\text{Al}} = 0.3, 0.5, 0.75, 1.0, 1.5$, and 2.0) were employed to study the SRO behaviors in $\text{Al}_x\text{CoCrFeNi}$ HEAs. Initial structures with these Al contents were generated by random substitution of elements for atomistic simulations, following the atomic number ratio of the examined compositions. $3 \times 3 \times 3$ FCC supercells (108 atoms) and $3 \times 3 \times 3$ BCC supercells (54 atoms) with random element distributions were employed for DFT calculations as in Fig. 1a, while $21 \times 21 \times 21$ FCC supercells (37,044 atoms) and $21 \times 21 \times 21$ BCC supercells (18,522 atoms) were used for classical MD simulations as in Fig. 1b. For each composition, using different seed values for random generator, multiple initial structures (at least five) with different configurations were generated for this study.

2.2. Atomistic Simulations: Classical molecular Dynamics, hybrid Monte-Carlo/Molecular Dynamics, and First-Principles calculations

Classical MD allows to simulate a large number of atoms and to obtain a long-time correlation, which is essential to reveal the structural and dynamic behaviors of the simulated materials at atomic scale. All the MD simulations were performed using large-scale molecular dynamics massively parallel simulator (LAMMPS) [35]. An embedded-atom-method (EAM) potential for Al-Cr-Co-Fe-Ni was employed to describe the atomic interactions [36]. Prior studies on the calculation of the phase stability as a function of Al, cohesive energy, elastic constants, and lattice distortions [36] demonstrate that this potential is reliable and accurate for modeling the thermodynamic properties of the HEA. An energy minimization was conducted for the relaxation of the initial structures, using the conjugate gradient (CG) algorithm. The minimization process was conducted until the maximum net atomic force was below 10^{-10} eV/Å and the energy change between successive iterations is less than 10^{-10} of the total energy. Periodic boundary conditions were applied to the x, y, and z directions, and the timestep was chosen as 1 fs. An isothermal, isobaric ensemble, *NPT* (constant number of atoms, constant pressure, and constant temperature) was employed to perform the relaxation under zero pressure. Then, switching the *NPT* ensemble to canonical *NVT* ensemble (constant number of atoms, volume, and temperature), simulations continued for 10 ns to produce the atomic data for the characterization of the materials. A Nosé-Hoover thermostat and barostat were applied to control the temperature and pressure, respectively [37,38].

Hybrid molecular dynamics/Monte Carlo (MD/MC) was employed to assess the short-range order in the HEAs. Random atomic swaps through MC led to the equilibration of the structure that cannot be obtained via conventional MD simulations. The hybrid MD/MC method was

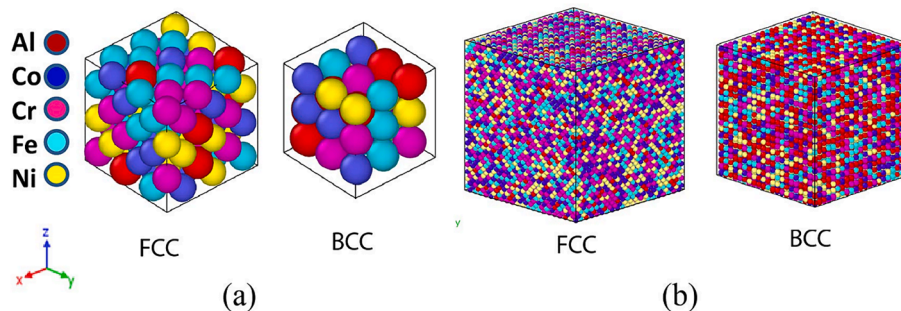


Fig. 1. (a) Initial $3 \times 3 \times 3$ supercell (FCC: 108 atoms and BCC: 54 atoms) for DFT calculations and (b) $21 \times 21 \times 21$ supercells (FCC: 37,044 atoms and BCC: 18,522 atoms) of $\text{Al}_x\text{CoCrFeNi}$ HEA structures for MD simulations.

employed here under the variance-constrained semi-grand canonical ensemble [39]. The acceptance of MC swap between two different types of atoms is determined by the Metropolis criterion. After an atomic swap, if the energy of the swapped configuration is lower than that of the configuration before the swap, the proposed swap is accepted. However, a swapped configuration with higher energy can also be accepted with an acceptance probability, $\exp(-\Delta E/k_B T)$, where ΔE represents the change in potential energy associated with the proposed swap, and k_B denotes the Boltzmann constant. In the hybrid MD/MC process, a single MC cycle, comprising 1,500 trial swaps for each atomic pair, was performed every 1,000 MD time steps. Given that there are 10 combinations of two dissimilar atomic types in five-element HEAs, a total of 15,000 MC swaps were attempted in one MC cycle. 1,500,000 MD time steps with a time step of 1 fs (equivalent to 1.5 ns) were executed for the hybrid MD/MC, resulting in 1,500 MC cycles and 22,500,000 MC swap attempts. Subsequently, bulk relaxations were performed via annealing for 1 ns employing the *NPT* ensemble, and the system will be equilibrated for another 500 ps, employing the *NVT* ensemble. During this process, the potential energy and the coordinates of the system were recorded.

First-principles calculations based on the density functional theory (DFT) were conducted to determine the equilibrium energy and lattice constant. All the DFT simulations were performed using Vienna *ab initio* simulation package (VASP) [40]. Periodic boundary conditions were applied in all directions. The projected augmented-wave (PAW) pseudo-potentials with the Perdew-Wang exchange–correlation were adopted here. A $2 \times 2 \times 2$ Γ -centered k -point sampling was used for the integration over the Brillouin zone. The plane-wave cutoff energy was set to 400 eV, and the electronic-convergence criterion was to 10^{-4} eV. The conjugate gradient method facilitated for the self-consistent calculation of the structure optimization. To identify and visualize crystalline order in atomic structures from both classical and quantum simulations, the common neighbor analysis (CNA) was conducted, using the Open Visualization Tool (OVITO) [41].

2.3. Characterization of HEAs

The Warren-Cowley (WC) parameter characterizes the degree of short-range order in $\text{Al}_x\text{CoCrFeNi}$ alloys. The WC parameter (α_{ij}) for two atom species i and j is calculated as [42]

$$\alpha_{ij} = 1 - \frac{p_{ij}}{c_j}, \quad (1)$$

where c_j is the molar fraction of the type j element, and p_{ij} is the probability of finding the j -type element around the i -type element in the nearest neighbor shell. The WC parameter is zero if $p_{ij} = c_j$, which indicates that there is no site preference between the i -type and j -type elements. The negative α_{ij} represents the increase in the number of i and j pairs, while the positive value corresponds to the opposite.

For comprehensive evaluation of the SRO effects, we examined different types of thermodynamic properties of the HEAs, which are the lattice thermal conductivity, coefficient of thermal expansion, and bulk modulus, representing the effectiveness of thermal transport, the structural response to temperature changes, and the structural response to mechanical stress, respectively. To calculate thermal conductivity, equilibrium molecular dynamics (EMD) simulations, where a finite, uniform temperature is applied to the simulation domain, were conducted using *NPT* ensemble for first 2 ns of the equilibration, followed by the *NVT* ensemble (constant number of particles, volume, and temperature) for the next 8 ns, resulting in a total simulation time of 10 ns. The last 5 ns of the resulting data were recorded and used to calculate the lattice thermal conductivity (k_L) by the Green-Kubo formula [43,44]:

$$k_L = \frac{V}{3k_B T^2} \int_0^\infty \langle J(0) \cdot J(t) \rangle dt, \quad (2)$$

where $\langle \rangle$ is the ensemble average, V is the equilibrium volume, and J is the heat-flux vector. Phonon density of states (D_p), which helps in understanding the behavior of lattice thermal conductivity, is calculated through the Fourier transform of the velocity autocorrelation function obtained from MD simulations [45].

The coefficient of thermal expansion (CTE) using the centered finite difference method as [46]

$$CTE = \frac{1}{3V(P, T)} \frac{V(P, T + \varepsilon) - V(P, T - \varepsilon)}{2\varepsilon}, \quad (3)$$

where ε represents an increment/decrement value of temperature (± 20 K).

The stiffness or elastic constants were determined from the stress–strain relation, as expressed by the Hooke's law [46,47],

$$C_{ij} = \frac{\sigma_i}{\varepsilon_j}, \quad (4)$$

where σ_i is the stress tensor, and ε_j is the strain tensor. Due to the cubic symmetry of FCC and BCC HEAs, only three independent elastic constants (C_{11} , C_{12} , and C_{44}) were identified. Subsequently, the bulk modulus (B) was determined using these elastic constants results from MD simulations [47,48]

$$B = \frac{C_{11} + 2C_{12}}{3}, \quad (5)$$

where C_{11} and C_{12} represent the elastic stiffness constants of a cubic single crystal.

Additionally, the B was also calculated, employing the Birch–Murnaghan equation of state and the average atomic energy with respect to the volume from the DFT calculations [49,50]:

$$E(V) = E_0 + \frac{9V_0 B}{16} \left\{ \left[\left(\frac{V_0}{V} \right)^{\frac{2}{3}} - 1 \right] B' + \left[\left(\frac{V_0}{V} \right)^{\frac{2}{3}} - 1 \right]^2 \left[6 - 4 \left(\frac{V_0}{V} \right)^{\frac{2}{3}} \right] \right\}, \quad (6)$$

where B' , and V_0 represent the derivative of the bulk modulus with respect to pressure, and the equilibrium volume, respectively.

3. Results and discussion

A previous study [33] on $\text{Al}_x\text{CoCrFeNi}$ HEAs confirmed that lower Al contents ($0 \leq x_{\text{Al}} \leq 0.75$) result in FCC structure while higher Al contents ($0.875 \leq x_{\text{Al}} \leq 2$) stabilize the BCC structure, which is aligned with this research; $x_{\text{Al}} = 0.3, 0.5$, and 0.75 for FCC and $x_{\text{Al}} = 1.0, 1.5$, and 2.0 for BCC. The distinct phases observed in the $\text{Al}_x\text{CoCrFeNi}$ HEAs can be attributed to the valence electron concentration (VEC), which is dependent on the chemical composition. VEC is regarded as one of the key factors determining the phase stability of the HEAs [51]. It is calculated using the atomic fraction and the VEC value of each individual element, denoted as c_i and $(\text{VEC})_i$ for element i , respectively, as $\text{VEC} = \sum_{i=1}^n c_i (\text{VEC})_i$ [51,52]. FCC solid solutions tend to form at $\text{VEC} > 7.8$, whereas BCC solid solutions are formed at $\text{VEC} < 7.35$ [51,53,54]. Our findings, revealing different concentration of element pairs in FCC and BCC phases, were aligned with this VEC analysis. Lower Al concentrations in $\text{Al}_{0.3}\text{CoCrFeNi}$ HEA, led to a higher VEC (> 7.8) for a strong FCC phase formation whereas higher Al concentrations led to lower VEC (< 7.35) indicating a strong BCC phase formation.

The atomic structures were relaxed to obtain the minimum energy structure, and thus the equilibrium lattice constant using DFT calculations and MD simulations. The calculated lattice constants (3.59 \AA for $x_{\text{Al}} = 0.3$, and 2.88 \AA for $x_{\text{Al}} = 2.0$) from our simulations are in a good agreement with the experimental results (3.59 \AA and 2.88 \AA , respectively) [55,56], as shown in Fig. 2.

High-entropy alloys exhibit different structural orders depending on

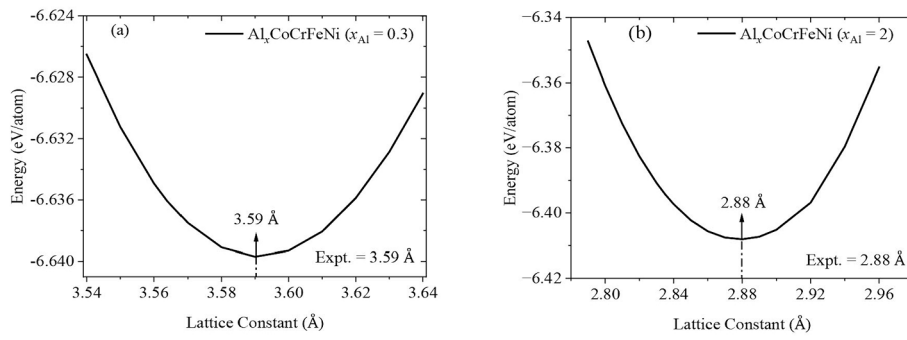


Fig. 2. Equilibrium lattice constant for FCC ($x_{\text{Al}} = 0.3$) and BCC ($x_{\text{Al}} = 2.0$) HEAs using DFT calculations. Lattice constants from the simulations agree well with the experimental measurements [55,56].

their atomic composition and configuration. Here, the Warren-Cowley (WC) parameters (α_{ij}) for various element pairs in $\text{Al}_x\text{CoCrFeNi}$ HEAs were calculated to understand such structural orders and their influence on the thermodynamic properties of the HEAs. Initial configurations of the HEAs for each atomic composition ($x_{\text{Al}} = 0.3, 0.5, 0.75, 1.0, 1.5$, and 2.0) were relaxed at room temperature (~ 300 K) using hybrid MD/MC simulations, and the initial and relaxed structures were then utilized to calculate the WC parameters for each element pair, within all FCC and BCC structures of $\text{Al}_x\text{CoCrFeNi}$ HEAs. The WC parameters for each element pair in all initial and relaxed structures for FCC and BCC HEAs are presented in Fig. 3.

Almost zero values of WC parameters were observed in the random configurations of both FCC ($x_{\text{Al}} = 0.3$) and BCC ($x_{\text{Al}} = 2.0$) HEA cases, indicating no specific preference for certain atom pairs [57]. After the MC relaxation process, the WC parameters of the Al-Fe and Al-Al were found to be most negative and most positive, respectively, in both FCC HEAs ($x_{\text{Al}} = 0.3$) and BCC HEAs ($x_{\text{Al}} = 2.0$), as illustrated in Fig. 3. Negative or lower WC parameters suggest a higher preference for the corresponding atom pair, indicating increased short-range ordering [57]. Therefore, Al-Fe was expected to be the dominant pairs for short-range ordering in the FCC and BCC HEAs. Conversely, the Al-Al pair was strongly unfavorable in both FCC and BCC HEAs. Apart from the dominant pairs, distinct SRO features were observed in FCC and BCC HEAs. Specifically, Al-Co was unfavorable while Co-Cr was favorable in the case of FCC HEAs, whereas the opposite trend was found for the BCC cases. Moreover, Al-Cr appeared to be unfavorable in FCC HEAs, whereas it did not have much impact in BCC HEAs. The opposite trend was found for the Co-Ni pair. Furthermore, Cr-Fe and Co-Fe pairs were unfavorable in both FCC and BCC HEAs.

To examine the effect of Al concentration on the SRO parameters,

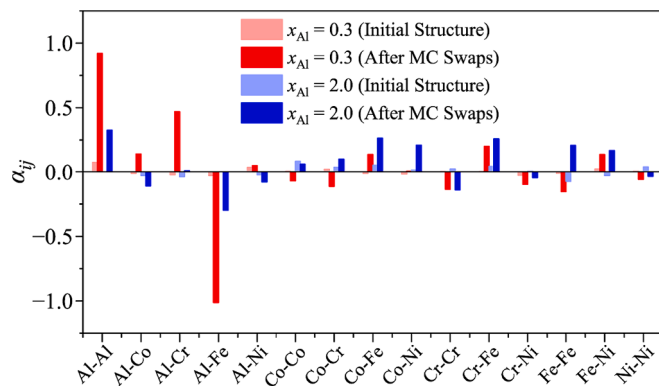


Fig. 3. Warren-Cowley (WC) parameters for the FCC ($x_{\text{Al}} = 0.3$) and BCC ($x_{\text{Al}} = 2.0$) HEAs. Initial structures with WC parameters close to zero demonstrate randomness. Higher negative values of WC parameters in HEAs after MC swaps indicate strong short-range ordering (SRO) in the HEAs.

various HEAs with different Al concentrations ($x_{\text{Al}} = 0.3, 0.5, 0.75, 1.0, 1.5$, and 2.0) were analyzed, as demonstrated in Fig. 4. A discernible pattern in the SRO parameters was observed here: as the Al content increases in the HEAs, the absolute value of WC parameters of favorable Al-Fe pair, while those of unfavorable Al-Al pair also decreased. Consequently, it can be stated that the intensity of SRO is higher in the FCC HEAs with lower Al contents, and the SRO becomes less pronounced in the BCC HEAs with higher Al contents.

The lattice thermal conductivities (k_L), coefficient of thermal expansion (CTE), and bulk modulus (B) of the $\text{Al}_x\text{CoCrFeNi}$ ($0 \leq x_{\text{Al}} \leq 2$) HEAs were evaluated via MD simulations using initial random configurations (denoted as ‘random’ or ‘without SRO’) and those after MC swaps showing more significant SRO (denoted as ‘SRO’ or ‘with SRO’). Bulk modulus was also calculated using DFT, and the obtained values exhibit good agreement with the MD results, as presented in Table 1. Moreover, the simulated bulk modulus values agree well with the experimental results of AlCoCrFeNi HEA [56]. This concurrence between MD, DFT, and experimental results not only supports the validity of our approaches, but also underscores the reliability of the EAM potential employed in this study, specifically in calculating thermodynamic properties using MD simulations.

Despite having identical atomic compositions, clear differences in thermodynamic properties between random and SRO structures have been observed, and these distinctions can be attributed to the different SROs. Fig. 5 demonstrates the effect of short-range order on the lattice thermal conductivity, i.e., with the SRO configurations of the HEAs, the lattice thermal conductivity is higher compared to the random configurations.

To further investigate the correlation between SRO and the lattice thermal conductivity, changes in the lattice thermal conductivity from initial random structures to SRO structures are presented with respect to the WC parameters for two selected pairs of SROs, $\alpha_{\text{Al-Fe}}$ and $\alpha_{\text{Al-Al}}$ in

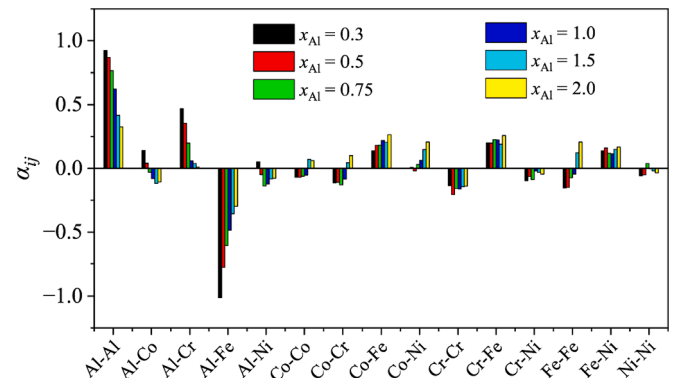


Fig. 4. WC parameters in the FCC ($x_{\text{Al}} = 0.3, 0.5$, and 0.75) and BCC ($x_{\text{Al}} = 1.0, 1.5$, and 2.0) HEAs after the MC swap process.

Table 1

Comparison of the lattice constant and bulk modulus of the $\text{Al}_x\text{CoCrFeNi}$ HEA from MD simulations and DFT calculations.

Configurations	Lattice Constant (Å)		Bulk Modulus (GPa)	
	MD Simulations	DFT Calculations	MD Simulations	DFT Calculations
FCC ($x_{\text{Al}} = 0.3$)	3.585	3.589	192.55	196.09
FCC ($x_{\text{Al}} = 0.5$)	3.538	3.536	183.55	180.79
FCC ($x_{\text{Al}} = 0.75$)	3.552	3.553	162.19	169.13
BCC ($x_{\text{Al}} = 1.0$)	2.841	2.839	151.28	152.07
BCC ($x_{\text{Al}} = 1.5$)	2.863	2.861	158.25	161.09
BCC ($x_{\text{Al}} = 2.0$)	2.875	2.882	148.36	156.84

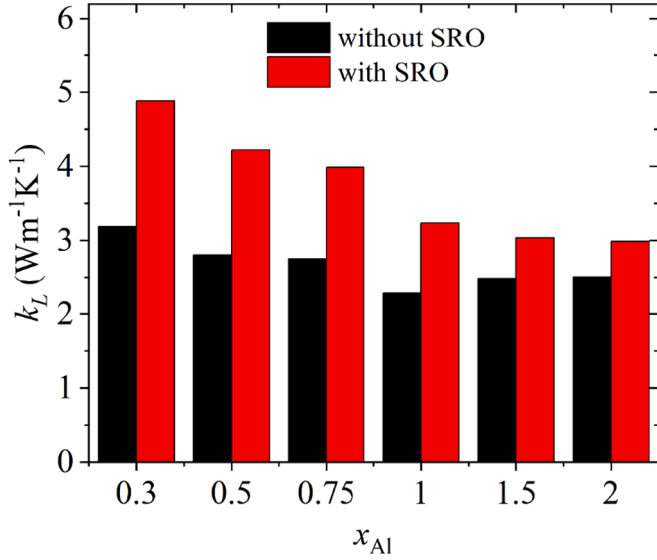
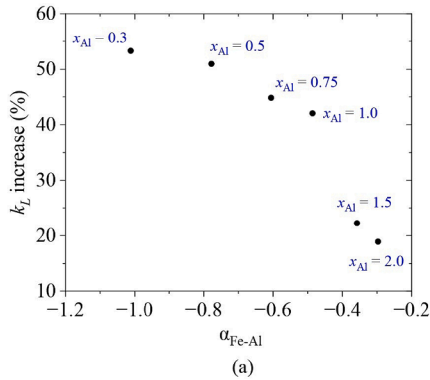


Fig. 5. Lattice thermal conductivity of $\text{Al}_x\text{CoCrFeNi}$ ($0 \leq x_{\text{Al}} \leq 2$) HEAs with random initial (without SRO) and MC swapped configurations (with SRO).

Fig. 6. The selected Al-Fe pair and Al-Al pair were chosen to represent the most negative and the most positive values of WC parameters within the SRO configurations, respectively, as shown in Fig. 4. Absolute values for both $\alpha_{\text{Al-Fe}}$ and $\alpha_{\text{Al-Al}}$ decrease with the increase of Al content in the HEAs, indicating reduced SROs, i.e., less preference or aversion and more random short-range order. A more than 50% increase in lattice thermal conductivity was observed at $x_{\text{Al}} = 0.3$, where the SRO intensity is maximum among all the HEAs. In contrast, at $x_{\text{Al}} = 2.0$, where SRO is not prominent compared to the random counterpart, the change in



lattice thermal conductivity is less than 20%.

Since phonon scattering is enhanced in more disordered structures [58], the higher lattice thermal conductivity in the SRO structures can be attributed to the increased structural order or a less extent of disorder. As shown in Fig. 7a and 7b, initial random structures without SRO have phonon density of states (or phonon spectra) with more broadened peaks compared to the SRO structures, allowing for an increased possibility of phonon-phonon interactions. These interactions scatter phonon transport, thereby reducing lattice thermal conductivity. Both FCC and BCC HEAs with SRO exhibit reduced broadening in phonon peaks. Specifically, the peak intensity of acoustic phonons, which are responsible for phonon transport, is increased as the Al content decreases. Thus, $\text{Al}_x\text{CoCrFeNi}$ HEAs exhibit higher thermal conductivity at lower Al contents, and accompanied by enhanced short-range orders.

The SRO configurations resulted in decreased thermal expansion coefficients as depicted in Fig. 8a. This decreasing trend contrasts with the case of lattice thermal conductivity. The calculated CTE values in this research are in reasonable agreement with the experimental results for $\text{Al}_x\text{CoCrFeNi}$ HEAs [55]. In addition to thermal expansion, the SRO also affects the bulk modulus of the HEAs. With the SRO configurations of the HEAs, the bulk modulus was found to be higher compared to the structures without SRO, as illustrated in Fig. 8b.

We attribute the reduction in thermal expansion coefficient and the increase in bulk modulus to the stronger atomic interactions in the SRO structures. The SRO structures, which result from the MC processes, are more energetically stable with stronger short-range atomic interactions. This leads to reduced sensitivity of structural changes to external temperature variations or mechanical pressure, that is, smaller thermal expansion and larger modulus can be induced. The changes in both the coefficient of thermal expansion and bulk modulus increase with the increasing WC parameters or more SRO in the configurations, similar to lattice thermal conductivity trend shown in Fig. 5. Finally, it can be stated that the properties of both FCC and BCC HEAs can be enhanced by tuning dominant element pairs according to their SRO parameters.

4. Conclusions

Thermodynamic properties of the HEAs and their correlation with local atomic ordering are crucial when designing efficient HEAs, however, this phenomenon was not explored in-depth yet. Thus, the effect of short-range order on lattice thermal conductivity, thermal expansion coefficient, and bulk modulus of the $\text{Al}_x\text{CoCrFeNi}$ HEAs ($0 \leq x_{\text{Al}} \leq 2$) was investigated using hybrid MD/MC simulations, classical MD simulations, and DFT calculations. The WC parameters were employed to characterize the ordering strength of the constituent element pairs in the $\text{Al}_x\text{CoCrFeNi}$ HEAs. From this study, Al-Fe was identified to be the most favorable pair, while Al-Al emerged as the most unfavorable pair among

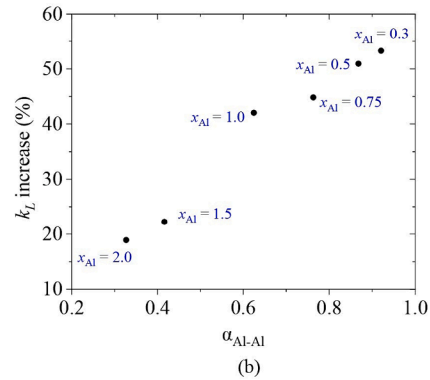


Fig. 6. (a) Highest increase in lattice thermal conductivity (k_L) can be observed for $\text{Al}_x\text{CoCrFeNi}$ HEA at $x_{\text{Al}} = 0.3$ with highest negative Al-Fe WC parameters and a decreasing trend can be observed with lower Al-Fe WC values. (b) Lowest increase in lattice thermal conductivity (k_L) can be observed at $x_{\text{Al}} = 2.0$ with the lowest positive Al-Al WC values and an increasing trend can be observed with higher Al-Al WC values.

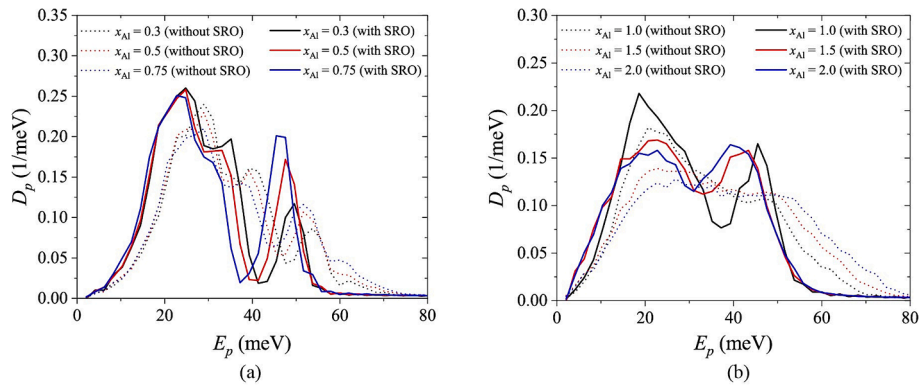


Fig. 7. Phonon density of states of (a) FCC $\text{Al}_x\text{CoCrFeNi}$ HEAs ($0 \leq x_{\text{Al}} \leq 0.75$) and (b) BCC $\text{Al}_x\text{CoCrFeNi}$ HEAs ($0.875 \leq x_{\text{Al}} \leq 2.0$) with random initial (without SRO) and MC swapped configurations (with SRO).

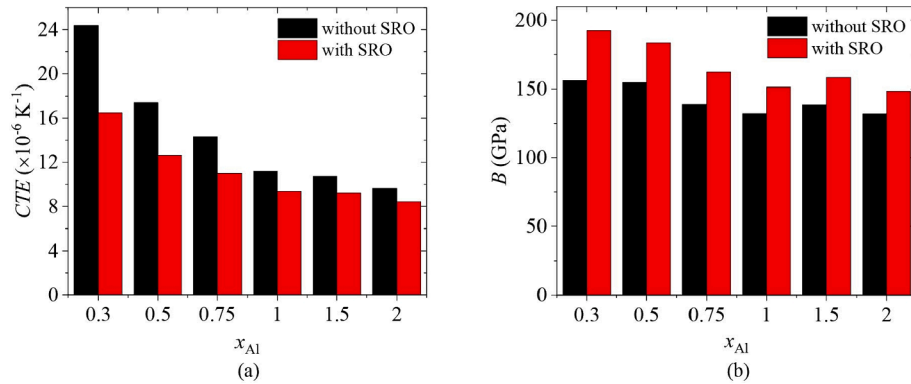


Fig. 8. (a) Coefficient of thermal expansion of $\text{Al}_x\text{CoCrFeNi}$ ($0 \leq x_{\text{Al}} \leq 2$) HEAs with random initial (without SRO) and MC swapped configurations (with SRO). (b) Bulk modulus of $\text{Al}_x\text{CoCrFeNi}$ ($0 \leq x_{\text{Al}} \leq 2$) HEAs with random initial (without SRO) and MC swapped configurations (with SRO).

all the HEAs. We observed that increasing the element pairs with higher SRO results in higher thermal conductivity, lower thermal expansion, and higher bulk modulus of the HEAs. These changes are attributed to the suppressed phonon-scattering and increased energetic stability induced by the enhanced SRO. The current work provides an insight into different interactions between element pairs and physical properties of the HEA. Therefore, this study will contribute to a quantitative theory-guided design strategy for selecting HEA elements and tuning composition to control the structural, chemical, and mechanical properties.

CRediT authorship contribution statement

Md Abdullah Al Hasan: Writing – original draft, Visualization, Validation, Software, Methodology, Investigation, Formal analysis, Data curation. **Seungha Shin:** Writing – review & editing, Writing – original draft, Supervision, Project administration, Methodology, Funding acquisition, Conceptualization. **Peter K. Liaw:** Resources, Funding acquisition, Conceptualization.

Declaration of competing interest

The authors declare that they have no known competing financial interests or personal relationships that could have appeared to influence the work reported in this paper.

Data availability

Data will be made available on request.

Acknowledgements

This work utilized the resources through allocation CTS170020 from the Advanced Cyberinfrastructure Coordination Ecosystem: Services & Support (ACCESS) program, which is supported by National Science Foundation grants #2138259, #2138286, #2138307, #2137603, and #2138296. PKL appreciates the supports from (1) the National Science Foundation (DMR – 1611180, 1809640, and 2226508) with program directors, Drs. J. Madison, J. Yang, G. Shiflet, and D. Farkas and (2) the US Army Research Office (FA9550-23-1-0503, W911NF-13-1-0438, and W911NF-19-2-0049) with program managers, Drs. M.P. Bakas, S.N. Mathaudhu, and D.M. Stepp.

References

- [1] Y.F. Ye, Q. Wang, J. Lu, C.T. Liu, Y. Yang, High-entropy alloy: challenges and prospects, *Mater. Today* 19 (2016) 349–362.
- [2] J.W. Yeh, S.K. Chen, S.J. Lin, J.Y. Gan, T.S. Chin, T.T. Shun, C.H. Tsau, S.Y. Chang, Nanostructured high-entropy alloys with multiple principal elements: novel alloy design concepts and outcomes, *Adv. Eng. Mater.* 6 (2004) 299–303.
- [3] E.J. Pickering, N.G. Jones, High-entropy alloys: a critical assessment of their founding principles and future prospects, *Int. Mater. Rev.* 61 (2016) 183–202.
- [4] B. Cantor, I.T.H. Chang, P. Knight, A.J.B. Vincent, Microstructural development in equiatomic multicomponent alloys, *Mater. Sci. Eng.: A* 213 (218) (2004) 375–377.
- [5] Y. Zhang, T.T. Zuo, Z. Tang, M.C. Gao, K.A. Dahmen, P.K. Liaw, Z.P. Lu, Microstructures and properties of high-entropy alloys, *Progr. Mater. Sci.* 61 (2014) 1–93.
- [6] L. Wang, F. Zhang, S. Yan, G. Yu, J. Chen, J. He, F. Yin, Microstructure evolution and mechanical properties of atmosphere plasma sprayed AlCoCrFeNi high-entropy alloy coatings under post-annealing, *J. Alloy. Compd.* 872 (2021) 159607.
- [7] C.C. Tasan, Y. Deng, K.G. Pradeep, M.J. Yao, H. Springer, D. Raabe, Composition dependence of phase stability, deformation mechanisms, and mechanical properties of the CoCrFeMnNi high-entropy alloy system, *JOM* 66 (2014) 1993–2001.

- [8] J.-W. Yeh, Alloy design strategies and future trends in high-entropy alloys, *JOM* 65 (2013) 1759–1771.
- [9] D.B. Miracle, O.N. Senkov, A critical review of high entropy alloys and related concepts, *Acta Mater.* 122 (2017) 448–511.
- [10] T. Egami, W. Guo, P.D. Rack, T. Nagase, Irradiation resistance of multicomponent alloys, *Metall. Mater. Trans. A* 45 (2014) 180–183.
- [11] I. Toda-Caraballo, J.S. Wróbel, S.L. Dudarev, D. Nguyen-Manh, P.E.J. Rivera-Díaz-del-Castillo, Interatomic spacing distribution in multicomponent alloys, *Acta Mater.* 97 (2015) 156–169.
- [12] R. Kozak, A. Sologubenko, W. Steurer, Single-phase high-entropy alloys – an overview, *Zeitschrift Für Kristallographie - Crystalline Materials* 230 (2015) 55–68.
- [13] M. Widom, W.P. Huhn, S. Maiti, W. Steurer, Hybrid Monte carlo/Molecular dynamics simulation of a refractory metal high entropy alloy, *Metall. Mater. Trans. A* 45 (2014) 196–200.
- [14] W. Feng, Y. Qi, S. Wang, Effects of short-range order on the magnetic and mechanical properties of FeCoNi(AlSi)_x high entropy alloys, *Metals* 7 (2017) 482.
- [15] S. Yin, J. Ding, M. Asta, R.O. Ritchie, Ab initio modeling of the energy landscape for screw dislocations in body-centered cubic high-entropy alloys, *Npj Comput. Mater.* 6 (2020) 110.
- [16] A. Tamm, A. Aabloo, M. Klintonberg, M. Stocks, A. Caro, Atomic-scale properties of Ni-based FCC ternary, and quaternary alloys, *Acta Mater.* 99 (2015) 307–312.
- [17] Q. Ding, Y. Zhang, X. Chen, X. Fu, D. Chen, S. Chen, L. Gu, F. Wei, H. Bei, Y. Gao, M. Wen, J. Li, Z. Zhang, T. Zhu, R.O. Ritchie, Q. Yu, Tuning element distribution, structure and properties by composition in high-entropy alloys, *Nature* 574 (2019) 223–227.
- [18] Q.-J. Li, H. Sheng, E. Ma, Strengthening in multi-principal element alloys with local-chemical-order roughened dislocation pathways, *Nat. Commun.* 10 (2019) 3563.
- [19] R.L. McGreevy, Reverse Monte Carlo modelling, *J. Phys. Condens. Matter.* 13 (2001) R877–R913.
- [20] Z. Lei, X. Liu, Y. Wu, H. Wang, S. Jiang, S. Wang, X. Hui, Y. Wu, B. Gault, P. Kontis, D. Raabe, L. Gu, Q. Zhang, H. Chen, H. Wang, J. Liu, K. An, Q. Zeng, T.-G. Nieh, Z. Lu, Enhanced strength and ductility in a high-entropy alloy via ordered oxygen complexes, *Nature* 563 (2018) 546–550.
- [21] X. Huang, X. Dong, L. Liu, P. Li, Liquid structure of Al-Si alloy: a molecular dynamics simulation, *J. Non Cryst. Solids* 503–504 (2019) 182–185.
- [22] E. Antillon, C. Woodward, S.I. Rao, B. Akdim, T.A. Parthasarathy, Chemical short range order strengthening in a model FCC high entropy alloy, *Acta Mater.* 190 (2020) 29–42.
- [23] M.A.A. Hasan, J. Wang, Y.C. Lim, A. Hu, S. Shin, Concentration dependence of hydrogen diffusion in α -iron from atomistic perspectives, *Int. J. Hydrogen Energy* 44 (2019) .27876–27884.
- [24] S.A. Uporov, R.E. Ryltsev, V.A. Bykov, S.K. Estemirova, D.A. Zamyatin, Microstructure, phase formation and physical properties of AlCoCrFeNiMn high-entropy alloy, *J. Alloy. Compd.* 820 (2020) 153228.
- [25] R. John, A. Karati, J. Joseph, D. Fabijanic, B.S. Murty, Microstructure and mechanical properties of a high entropy alloy with a eutectic composition (AlCoCrFeNi_{2.1}) synthesized by mechanical alloying and spark plasma sintering, *J. Alloy. Compd.* 835 (2020) 155424.
- [26] G. Shang, L. Jiang, Z.-Z. Liu, X.-G. Lu, High-throughput experimental study on the microstructural and compositional variations of mechanical properties for AlCoCrFeNi high entropy alloys, *J. Alloy. Compd.* 917 (2022) 165513.
- [27] D. Modupeola, P. Patricia, A. Samson, and M. Ntombi, High Entropy Alloys for Aerospace Applications, in: G.-B. Mofid, A. Aly-Mousaad (Eds.), *Aerodynamics*, IntechOpen, Rijeka, 2019, p. Ch. 7.
- [28] X. Yan, Y. Zhang, Functional properties and promising applications of high entropy alloys, *Scr. Mater.* 187 (2020) 188–193.
- [29] H. Ren, R.R. Chen, X.F. Gao, T. Liu, G. Qin, S.P. Wu, J.J. Guo, High-performance AlCoCrFeNi high entropy alloy with marine application perspective, *J. Mater. Res. Technol.* (2023) 256751–256763.
- [30] Y. Geng, H. Tan, L. Wang, A.K. Tieu, J. Chen, J. Cheng, J. Yang, Nano-coupled heterostructure induced excellent mechanical and tribological properties in AlCoCrFeNi high entropy alloy, *Tribol. Int.* 154 (2021) 106662.
- [31] L.J. Santodonato, P.K. Liaw, R.R. Unocic, H. Bei, J.R. Morris, Predictive multiphase evolution in Al-containing high-entropy alloys, *Nat. Commun.* 9 (2018) 4520.
- [32] A. Sharma, P. Singh, D.D. Johnson, P.K. Liaw, G. Balasubramanian, Atomistic clustering-ordering and high-strain deformation of an Al_{0.1}CrCoFeNi high-entropy alloy, *Sci. Rep.* 6 (2016) 31028.
- [33] M.A.A. Hasan, J. Wang, S. Shin, D.A. Gilbert, P.K. Liaw, N. Tang, W.L.N. C. Liyanage, L. Santodonato, L. DeBeer-Schmitt, N.P. Butch, Effects of aluminum content on thermoelectric performance of Al_xCoCrFeNi high-entropy alloys, *J. Alloy. Compd.* 883 (2021) 160811.
- [34] Z. Sun, C. Shi, L. Gao, S. Lin, W. Li, Thermal physical properties of high entropy alloy Al_{0.3}CoCrFeNi at elevated temperatures, *J. Alloy. Compd.* 901 (2022) 163554.
- [35] S. Plimpton, Fast parallel algorithms for short-range molecular dynamics, *J. Comput. Phys.* 117 (1995) 1–19.
- [36] D. Farkas, A. Caro, Model interatomic potentials for Fe–Ni–Cr–Co–Al high-entropy alloys, *J. Mater. Res.* 35 (2020) 3031–3040.
- [37] D.J. Evans, B.L. Holian, The nose-hoover thermostat, *J. Chem. Phys.* 83 (1985) 4069–4074.
- [38] G.J. Martyna, D.J. Tobias, M.L. Klein, Constant pressure molecular dynamics algorithms, *J. Chem. Phys.* 101 (1994) 4177–4189.
- [39] B. Sadigh, P. Erhart, A. Stukowski, A. Caro, E. Martinez, L. Zepeda-Ruiz, Scalable parallel Monte Carlo algorithm for atomistic simulations of precipitation in alloys, *Phys. Rev. B* 85 (2012) 184203.
- [40] G. Kresse, J. Furthmüller, Efficient iterative schemes for *ab initio* total-energy calculations using a plane-wave basis set, *Phys. Rev. B* 54 (1996) 11169–11186.
- [41] A. Stukowski, Visualization and analysis of atomistic simulation data with OVITO—the open visualization tool, *Model. Simul. Mater. Sci. Eng.* 18 (2010) 015012.
- [42] J.M. Cowley, Short-range order and long-range order Parameters, *Phys. Rev.* 138 (1965) A1384–A1389.
- [43] M.S. Green, Markoff random processes and the statistical mechanics of time-dependent phenomena. II. irreversible processes in fluids, *J. Chem. Phys.* 22 (1954) 398–413.
- [44] R. Kubo, Statistical-mechanical theory of irreversible processes. I. General theory and simple applications to magnetic and conduction problems, *J. Phys. Soc. Jpn.* 12 (1957) 570–586.
- [45] S. Shin, M. Kaviani, T. Desai, R. Bonner, Roles of atomic restructuring in interfacial phonon transport, *Phys. Rev. B* 82 (2010) 081302.
- [46] H. Nejat Pishkenari, E. Mohagheghian, A. Rasouli, Molecular dynamics study of the thermal expansion coefficient of silicon, *Phys. Lett. A* 380 (2016) 4039–4043.
- [47] G. Clavier, N. Desbiens, E. Bourasseau, V. Lachet, N. Brusselle-Dupend, B. Rousseau, Computation of elastic constants of solids using molecular simulation: comparison of constant volume and constant pressure ensemble methods, *Mol. Simul.* 43 (2017) 1413–1422.
- [48] S.M. Rassoulinejad-Mousavi, Y. Mao, Y. Zhang, Evaluation of copper, aluminum, and nickel interatomic potentials on predicting the elastic properties, *J. Appl. Phys.* 119 (2016) 244304.
- [49] F. Birch, Finite elastic strain of cubic crystals, *Phys. Rev.* 71 (1947) 809–824.
- [50] F. Murnaghan, The compressibility of media under extreme pressures, *PNAS* 30 (9) (1944) 244–247.
- [51] S. Guo, C. Ng, J. Lu, C.T. Liu, Effect of valence electron concentration on stability of FCC or BCC phase in high entropy alloys, *J. Appl. Phys.* 109 (2011) 103505.
- [52] S. Guo, C.T. Liu, Phase stability in high entropy alloys: Formation of solid-solution phase or amorphous phase, *Progress in Natural Science: Materials International* 21 (2011) 433–446.
- [53] G. Zhang, X. Yang, W. Qi, Y. Li, W. Wang, Y. Chen, J. Li, L. Li, Effect of co on phase stability and mechanical behavior of CoCrFeNiMnAl_{0.3} high entropy alloys with micro/nano hierarchical structure, *Mater. Des.* 215 (2022) 110442.
- [54] Y. Ma, Q. Wang, B.B. Jiang, C.L. Li, J.M. Hao, X.N. Li, C. Dong, T.G. Nieh, Controlled formation of coherent cuboidal nanoprecipitates in body-centered cubic high-entropy alloys based on Al₂(Ni Co, Fe, Cr)₁₄ compositions, *Acta Mater.* 147 (2018) 213–225.
- [55] H.-P. Chou, Y.-S. Chang, S.-K. Chen, J.-W. Yeh, Microstructure, thermophysical and electrical properties in Al_xCoCrFeNi (0 ≤ x ≤ 2) high-entropy alloys, *Mater. Sci. Eng. B* 163 (2009) 184–189.
- [56] B. Cheng, F. Zhang, H. Lou, X. Chen, P.K. Liaw, J. Yan, Z. Zeng, Y. Ding, Q. Zeng, Pressure-induced phase transition in the AlCoCrFeNi high-entropy alloy, *Scr. Mater.* 161 (2019) 88–92.
- [57] X. Huang, L. Liu, X. Duan, W. Liao, J. Huang, H. Sun, C. Yu, Atomistic simulation of chemical short-range order in HfNbTaZr high entropy alloy based on a newly-developed interatomic potential, *Mater. Des.* 202 (2021) 109560.
- [58] F. Körmann, Y. Ikeda, B. Grabowski, M.H.F. Sluiter, Phonon broadening in high entropy alloys, *Npj Comput. Mater.* 3 (2017) 36.